RSC Advances

ROYAL SOCIETY OF CHEMISTRY

www.rsc.org/advances

Cite this: DOI: 10.1039/c0xx00000x

www.rsc.org/xxxxxx

ARTICLE TYPE

Green Synthesis and Catalytic Performance of Nanoscale CeO_2 Sheets

Guoqing Zhang*, Ju Ao, Yili Guo, Zhaoxia Zhang, Min Shao, Lina Wang, Lan Zhou, Jianzhong Shao

Received (in XXX, XXX) Xth XXXXXXXXX 20XX, Accepted Xth XXXXXXXXX 20XX
DOI: 10.1039/b000000x

ABSTRACT: Nano-thick CeO_2 sheets were synthesized by a facile and green hydrothermal precipitation method in the strong alkali solution. The experimental results indicate, without any surfactant and template, nanoscale thick CeO_2 sheets can be successfully synthesized just by adding cerium nitrate into ammonia at room temperature. The Rietveld refinement analysis demonstrates that the synthesized CeO_2 sheets have more defect structure than that of nanoparticles and rods. The photocatalytic performance of the CeO_2 sheets was also evaluated by decomposing an azo dye, methyl orange. Compared with nanoparticles and rods, the synthesized CeO_2 nanosheets exhibit higher photocatalytic activity during the degradation.

1. Introduction

In last decades, ceria (CeO_2) has been a research focus because of its wide applications, such as solid oxide fuel cells[1], production and purification of hydrogen, catalytic materials for three-way catalyst (TWC) and fluid catalytic cracking (FCC)[2], optical and dielectric materials[3-5] and buffer layer for oxide superconductors[6-10]. Especially, CeO_2 has been extensively studied as active or support catalytic materials owing to its superior oxygen storage-and-release properties[11]. CeO_2 can provide lattice oxygen in chemical reactions due to lower formation energy for oxygen vacancy as a good electron acceptor[12-14], it also promotes the chemical activity of the material by facilitating electron transfer from suitable adspecies into oxide surface[15,16].

In many recent studies[17-20], a higher catalytic activity was revealed in defect-rich ceria nanoparticles, which is relative to the type, size, and distribution of oxygen vacancies as the most relevant surface defects. In fact, surface defects more readily form in respect of those CeO_2 nanocrystals with special morphology, such as cube, nanowire and nanotube and so on. In addition, multi-dimensional CeO_2 nanomaterials, like one-dimensional (1D) rod or wire and two-dimensional (2D) sheet, are intensively investigated owing to novel physical properties and potential applications. So far, 1D CeO_2 such as nanorods[21-24], nanowires[25-28], nanotubes[29-33], have been successfully fabricated by various chemical or physical methods. However, 2D ceria sheet, especially those with nanoscale thickness, still is difficult to prepare under present conditions.

Yu Y.F. *et al*. rported the preparation of ultrathin CeO_2 nanosheets through the thermal decomposition of single-layered $Ce(OH)CO_3$[34]. Ko JW *et al*. synthesized nano-grained CeO_2 sheets using polydopamine-induced $CaCO_3$ vaterite microspheres[35]. Their research results indicate CeO_2 sheets have better photocatalytic performance than that of particles.

However, above preparation methods of CeO_2 nanomaterials (including particles, rods, wires and sheets etc.) are complicated and generally need special chemicals and strict experimental conditions. Nowadays, the environmental issue is of concern when carrying out a chemical synthesis. It is very necessary to develop green synthesis technology for CeO_2 nanomaterials. We recently developed a facile chemical solution deposition (CSD) method to prepare nanothick CeO_2 sheets, the experimental results suggest that CeO_2 sheets can be successfully synthesized just by adding cerium nitrate into ammonia at room temperature, which actually is a green synthesis route owing to no any surfactant added and the final product can be obtained by washing the precipitates with water. The subsequent photodegradation experiments demonstrate that the CeO_2 sheets show higher catalytic activity than that of CeO_2 particles and rods.

2. Experimental Section

2.1 Preparation and characterization

In a typical synthesis, 10 ml 0.05 mol/L cerium nitrate ($Ce(NO_3)_3$•$6H_2O$) solution was dropped precisely into 40 ml ammonia solution under magnetic stirring at room temperature. The suspension was then held at room temperature for 2 hrs with faint yellow precipitates appearing slowly. The resultant product was washed several times with distilled water and then dried at 80 ℃ for 2 hrs. At the same time, as counterparts, CeO_2 particles

and rods were prepared according to the method reported in our previous research[36].

X-ray powder diffraction testing was performed on a Thermo ARL X-ray powder diffractometer to analyze the microstructure of the product. The morphology of the CeO_2 product was observed by High Resolution Electron Microscope (HRSEM, Carl Zeiss SMT ULTRA-55) by ultrasonic dispersing or directly adhering the obtained powder on the sample stage. Transmission Electron Microscope (TEM, JEOL JSM-2100) and Atomic Force Microscopy (AFM, Park Systems, XE-110E) were used to observe facial microstructure, respectively. The UV-Vis spectra data of the samples were also recorded on a UV-Vis spectrophotometer (Hitachi U-3010) in order to estimate the band gap energy of the CeO_2 nanomaterials. In addition, Brunauer–Emmet–Teller specific surface area (S_{BET}) and micropore volume (Wo) of the CeO_2 particles, rods and sheets were also determined using a high-speed automated area and pore size analyzer.

2.2 Photocatalytic procedures

The photocatalytic experiments were conducted in a magnetically stirred Pyrex reactor. The light source was a 300 W xenon–mercury lamp with a wavelength of 254 nm. In a typical experiment, an aqueous methyl orange (50mL, 100μM) was mixed with 0.05 g of CeO_2 photocatalyst (particles, rods or sheets respectively) in a beaker. The above suspensions were poured into the reactor and magnetically stirred for two hours to obtain absorption equilibrium prior to UV irradiation. After the UV irradiation starting, aliquots of samples were taken at a regular interval and filtrated for measurement of the decoloration rate of the dye using the Hitachi U-3010 UV–vis spectrometer.

In the catalytic reaction process, a few specimens were sucked up and mixed with 0.04 mol/L DMPO for Electron Paramagnetic Resonance (EPR) testing. EPR signals of radicals trapped by DMPO were recorded at ambient temperature on a Bruker E500 spectrometer.

3. Results and Discussion

The experimental results disclose that CeO_2 morphology strongly depends on the pH value of the starting ammonia solution, CeO_2 sheets can just take shape in the strong alkali condition (pH>12). In fact, purple $Ce(OH)_3$ precipitates first generated within an initial reaction period, soon the color of the suspension changed into faint yellow with CeO_2 forming. After aged for two hours, the final product was washed using distilled water and dried to be faint yellow powder. The morphology of the CeO_2 powder was first observed by HRSEM and TEM. A few separated sheets (from the dispersed specimen) and a cluster of sheets (from powder specimen) can be seen from Figure 1 a and b, respectively. More clearly, a picec of CeO_2 sheet with nice and uniform appearance can be observed from a TEM image as shown in Figure 1 c. The HRTEM graph of a piece of sheet is shown in Figure 1 d, the spacing between two adjacent lattice plane is calculated to be around 0.316 nm, which corresponds to the (111) lattice plane of CeO_2. The inset SAED (Selected Area Electron Diffraction) pattern confirms the polycrystalline nature of the sample, and the exposed planes are mainly attributed to (111) reflection. Atomic force microscopy (AFM) was then employed to measure the thickness of the CeO_2 sheet, and it is recorded to be a dozen nanometers by line scan as seen in Figure 1 f.

The formation of the nanosheets is usually a direct sequence of "orientment attachment" growth of the nanocrystals[37]. Oriented attachment involves spontaneous self-organization of adjacent particles, the nanocrystals can share a common crystallographic orientation and extend at a planar interface. According to above mechanism, CeO_2 nanocrystals grew up along active planes (100) or (110), while (111) mostly exposed outside of the surface.

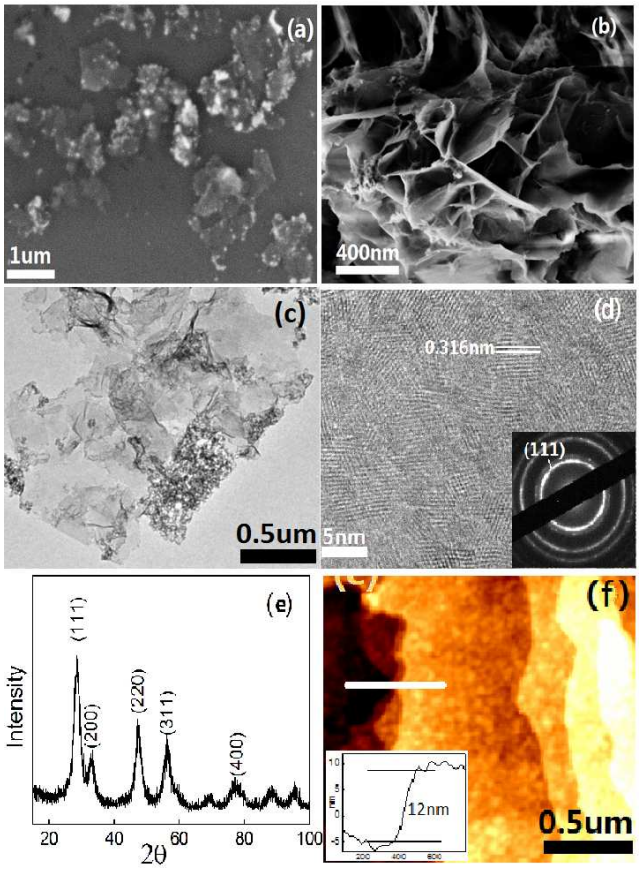

Figure 1 HRSEM images of the synthesized CeO_2 sheets, (a) a few sheets and (b) a cluster of sheets. (c) is TEM image of a piece of sheet, and (d) is corresponding HRTEM graph with insert SAED diffraction ring. (e) the XRD pattern of the sheets with several special diffraction reflections of (111), (200), (220), (311) and (400). AFM image (f) shows a piece of sheet with a dozen nanometers in thickness according to the height profile taken along the white straight line.

The XRD pattern of the synthesized CeO_2 sheets is shown in Figure 1 d. A series of diffraction peaks are just corresponding to the (111), (200), (220), (311), (331), (420) and (422) reflections of a cubic fluorite structure CeO_2 (ICSD, 88759). The diffraction data of the CeO_2 sheets, including particles and rods, were refined using the Rietveld refinement method on a Maud software (Version 2.33), and the lattice parameters, crystallite sizes and intrinsic default probability were calculated and listed in Table 1. Figure 2 shows the refinement results of the CeO_2 sheets, which

is fitted well with a lower R_w value and straight difference line. From the refinement results of the three samples, the grain size decreases significantly from 6.1 nm for particles to 3.8 nm for sheets, while the intrinsic default probability increases moderately. The fault probability, determined by Warren model, actually varies inversely with crystallite size according to Warren equations. The three-dimensional inset, shown as an octahedral shape in Figure 2, is the fitted structural model of a CeO_2 crystalline grain. It is clear that the exposed plane is mostly (111) reflection, and atomistic simulation study demonstrates there is a higher facility for the generation of associated vacancy defects on (111) surfaces in comparison with (110) and (100) ones[38]. Which means the nanomaterials with more exposed (111) reflection have higher reactivity when acting as a functional material.

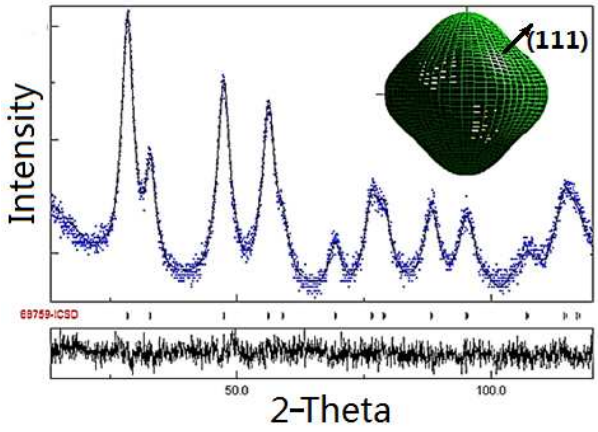

Figure 2 Rietveld refinement pattern of the CeO_2 sheets, below is a different line and three-dimensional structural model of a CeO_2 crystalline grain is shown on top right.

Table 1 XRD refinement and specific area measurement results of the ceria particles, rods and sheets.

	Particles	Rods	Sheets
a, Å	5.4219 (6)	5.4212 (5)	5.4208 (4)
Default probability, %	1.22 (3)	1.78 (5)	1.98 (4)
Mean grain size, nm	6.1 (3)	5.0 (2)	3.8 (3)
R_w %	8.52	9.32	9.03
S_{BET}, m^2/g	166.8	180.5	161.6
W_0,ml/g	0.341	0.406	0.347

In addition, as key parameters for nanomaterial, specific area (S_{BET}) and pore volume (W_o) of these nanomaterials were measured and listed in Table 1. All of the CeO_2 nanomaterials exhibit high specific area (over 160 m^2/g) and pore volume (over 0.34 ml/g) owing to their smaller particle size or special morphology. Of all, owing to smaller crystallite and particle size, CeO_2 nanorods have largest specific area and pore volume with 180.5 m^2/g and 0.406 ml/g, respectively. The nanosheets, having the smallest grain size but largest particle size, also exhibit large specific area and pore volume comparable to that of the spherical particles. Specific area actually plays an important role when used as functional material, especially as catalytic material, which directly affects the catalytic efficiency of the catalyst.

Light absorption properties, corresponding to the photocatalytic activity, is very important for a nanomaterial catalyst. Form the UV absorption spectra shown in Figure 3 (a), the absorption peaks of CeO_2 nanoscale particles, rods and sheets are located at 290, 304 and 306 nm, respectively. And a red shift in the UV absorption spectra was observed with their morphology transformed from sphere to rod and sheet owing to the quantum size effect[39].

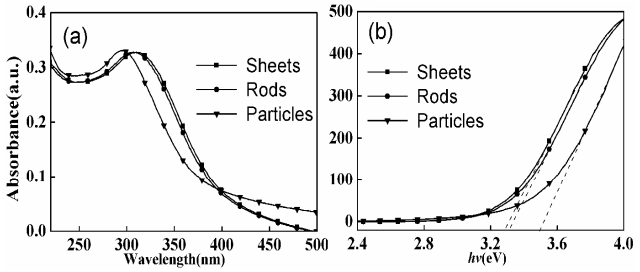

Figure 3 (a) UV spectra of the synthesized nanomaterials and (b) the plots of $(\alpha hv)^2$ versus hv.

The band gap energies for the CeO_2 nanoparticles, nanorods and nanosheets were estimated to be 3.41, 3.30 and 3.26 eV, respectively, by extrapolating the linear portions of the curves to the zero absorption line on the plots of $(\alpha hv)^2$ versus hv as shown in Figure 3 b. Clearly, nanosheets exhibit lowest band gap energy owing to its smaller grain size, which may be more easily photogenerated in a photocatalytic process.

The knowledge of the defect structure contained on the CeO_2 surface is inevitable towards deep understanding of its reactivity. Planar stacking faults are a common defect in crystals, which is closely relative with the morphology of the nanomaterials. Above results demonstrate that multidimensional CeO_2 nanomaterials, such as rod and sheet, have more defects owing to close-packing of the smaller grains. For CeO_2 nanomaterials, most defects are due to oxygen vacancy and stacking dislocation. Therefore the CeO_2 sheets, with more surface defects, maybe have stronger catalyst activity compared with that of the particles and rods. In order to clarify the point, the photocatalytic performance of the spherical, rodlike and sheet CeO_2 is evaluated by degrading methyl orange, a persistent azo dye, under UV irradiation.

The absorption percentages of methyl orange on the three CeO_2 nanomaterials were first recorded by measuring the concentration of the dye before and after absorption equilibrium on a UV spectrometer. It is clear that different morphology CeO_2 shows different absorption ability, CeO_2 rods can absorb more dye (about 9.0 %) owing to its higher specific area of 180.5 m^2/g while sheets and particles have about 8.3 % absorption capacity with specific area 161.6 and 166.8 m^2/g, respectively. In next photodegradation experiments, after excluding the absorption effect, the degradation percentages of the catalysts were measured and calculated by recording absorbance spectrum of all the specimens and then normalized the absorption curves. The results together with trendlines were exhibited in Figure 4.

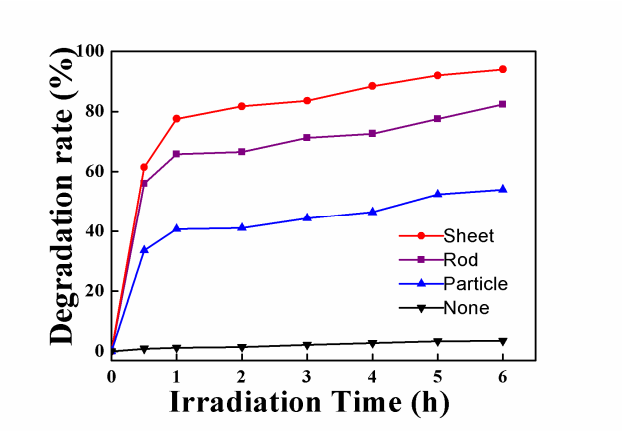

Figure 4 The plots of degradation percentage *vs* irradiation time for photodegradation of methyl orange with or without CeO_2 catalysts.

Figure 4 exhibits the processes of photogradation of the three CeO_2 catalysts with increasing UV irradiation time. After 6 hours' reaction, comparing to catalyst-free, the addition of CeO_2 catalysts obviously promotes the degradation of methyl orange, and the CeO_2 sheets show strongest catalytic ability with about 92% degradation percentage, and then rods and particles with 78% and 51%, respectively. At the same time, it can be observed from the plots that the photocatalytic degradation process mainly occurred in the initial phase of the catalytic reaction. Undoubtedly, the catalytic results confirmed the above relationship between catalysis morphology and its catalytic ability.

EPR experiments were carried out to examine photoinduced process taking place in the catalytic oxidation. A set of experiments focuses on the capability of these CeO_2 to photogenerate OH · radicals. For this purpose, aqueous suspensions of the CeO_2 samples were irradiated in the presence of a typical radical spin trap molecule (DMPO).

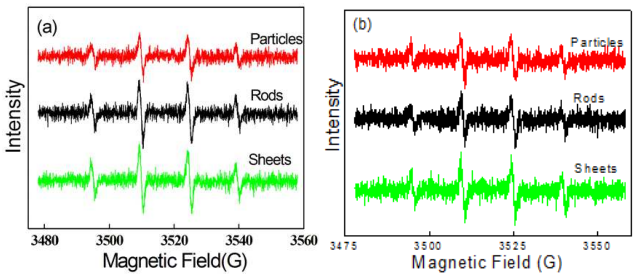

Figure 5 EPR spectra of the DMPO-sample aqueous suspensions after (a) 10 mins and (b) 60 mins UV irradiation.

The EPR spectra recorded in Figure 5 show that there is exclusively give rise to a 1:2:2:1 quartet signal in every EPR spectra for all the DMPO-containing aqueous suspensions. Noteworthy, a higher intensity of these species is detected in the suspension of CeO_2 sheets in comparison with that of particles and rods, when suffering 10 mins and even 60 min irradiation. This suggests that a higher concentration of surface hydroxyl radicals is produced during the photocatalytic degradation when using CeO_2 sheets as catalyst, which is the reason for its stronger catalytic performance.

The reusability of the sheet CeO_2 photocatalyst for the degradation of methyl orange was evaluated by recovering and photodegradation repeatedly. The CeO_2 sheets were first separated and collected from the suspension using a centrifuge. Owing to its larger grain, the CeO_2 sheets is very easily regained and there is almost no any loss in comparison with the original amount by exactly weighing the dried precipitates, which avoid the second pollution resulted from photocatalyst itself. The CeO_2 sheets were reused just after washing with water and the catalytic activity of the recovered catalyst was found to be close to the fresh catalyst even suffered three cycles of reactions. Figure 6 shows three cycles photocatalytic degradation curves by using repeatedly sheet CeO_2 catalyst to decompose methyl orange. Degradation percentage of methyl orange of each cycle is up to that of first use after six hours' UV irradiation, but the degradation rate obviously decreases because of the residual dye adsorbing on the surface of the CeO_2 sheets. Shimizu *et al.*[40] found in their recent research that CeO_2 is a most suitable catalyst in terms of catalytic activity reusability and leaching-resistance. Above results indicate, as a nanoscale catalytic material with large specific area, CeO_2 sheets would be very promising in application of photocatalytic degradation.

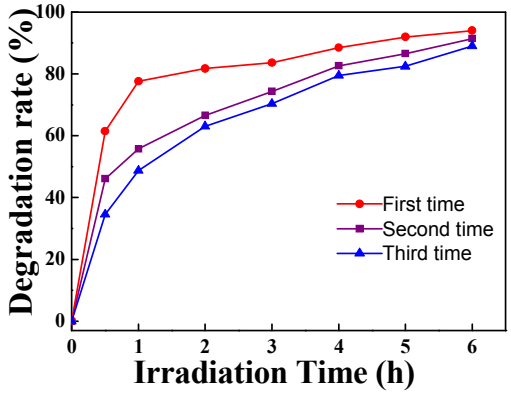

Figure 6 The photodegradation curves of three cycles for methyl orange with CeO_2 sheets as catalyst.

4. Conclusions

In the present study, a facile and green hydrothermal precipitation method was established to synthesize nanoscale CeO_2 sheets by self-organization under hydrothermal condition. No any surfactant was added and harmful matter producd during the synthesis. The results show fine CeO_2 sheets with a dozen nanometers thickness can be synthesized in strong alkali solution. The microstructure and morphology of ceria sheets were then studied by XRD, HSEM, TEM and AFM. The fault probabilities of particles, rods and sheets were calculated using Warren model, and the refinement results exhibit the ceria sheets have a higher

fault probability owing to rich defects on the surface.

Above results provide direct information on the sheet morphology and surface defects which are usually considered as active sites for catalysis over ceria. Subsequent photocatalytic degradation experiments for methyl orange indicate that the catalytic performance of CeO_2 nanomaterials is closely related to their morphology. CeO_2 sheets, owing to more surface defects, exhibit higher catalytic activity compared with particles and rods. Furthermore, its reusability was also demonstrated to be good after multi-cycles photodegradation experiments.

Notes and references

Key Laboratory of Advanced Textile Materials and Manufacturing Technology, Zhejiang Sci-Tech University, Ministry of Education, Hangzhou 310018, P. R. China.

Corresponding Author
** Tel: +86-571-86843588. Fax: +86-571-86843629. E-mail: zgq@zstu.edu.cn*

ACKNOWLEDGMENT

The work was financially supported by the National Natural Science Foundation of China under Grant No. 51073142 and Zhejiang Provincial Natural Science Foundation under Grant No. LY13E030004. The authors also acknowledge the support from Zhejiang Provincial Top Key Academic Discipline of Chemical Engineering and Technology.

References

1. S. D. Park, J. M. Vohs and R. J. Gorte, *Nature*, 2000, **404**, 265-267.
2. A. Trovarelli, C. de Leitenburg, M. Boaro and G. Dolcetti, *Catal Today*, 1999, **50**, 353-367.
3. A. Trovarelli, *Catal Rev*, 1996, **38**, 439-520.
4. E. P. Murray, T. Tsai and S. A. Barnett, *Nature*, 1999, **400**, 649-651.
5. P. Patsalas, S. Logothetidis, L. Sygellou and S. Kennou, *Phys Rev B*, 2003, **68**, 035104.
6. J. D. Budai, W. G. Yang, N. Tamura, J. S. Chung, J. Z. Tischler, B. C. Larson, G. E. Ice, C. Park and D. P. Norton, *Nat Mater*, 2003, **2**, 487-492.
7. S. N. Jacobsen, L. D. Madsen and U. Helmersson, *J Mater Res*, 1999, **14**, 2385-2393.
8. F. Sandiumenge, A. Cavallaro, J. Gazquez, T. Puig, X. Obradors, J. Arbiol and H. C. Freyhardt, *Nanotechnology*, 2005, **16**, 1809-1813.
9. A. Cavallaro, F. Sandiumenge, J. Gazquez, T. Puig, X. Obradors, J. Arbiol and H. C. Freyhardt, *Adv Funct Mater*, 2006, **16**, 1363-1372.
10. S. Engel, K. Knoth, R. Huhne, L. Schultz and B. Holzapfel, *Supercond Sci Tech*, 2005, **18**, 1385-1390.
11. G. A. Deluga, J. R. Salge, L. D. Schmidt and X. E. Verykios, *Science*, 2004, **303**, 993-997.
12. M. Nolan, S. C. Parker and G. W. Watson, *Surf Sci*, 2005, **595**, 223-232.
13. M. V. Ganduglia-Pirovano, J. L. F. Da Silva and J. Sauer, *Phys Rev Lett*, 2009, **102**.
14. A. Migani, G. N. Vayssilov, S. T. Bromley, F. Illas and K. M. Neyman, *Chem Commun*, 2010, **46**, 5936-5938.
15. G. N. Vayssilov, Y. Lykhach, A. Migani, T. Staudt, G. P. Petrova, N. Tsud, T. Skala, A. Bruix, F. Illas, K. C. Prince, V. Matolin, K. M. Neyman and J. Libuda, *Nat Mater*, 2011, **10**, 310-315.
16. M. Baron, H. Abbott, O. Bondarchuk, D. Stacchiola, A. Uhl, S. Shaikhutdinov, H. J. Freund, C. Popa, M. V. Ganduglia-Pirovano and J. Sauer, *Angew Chem Int Edit*, 2009, **48**, 8006-8009.
17. S. Carrettin, P. Concepcion, A. Corma, J. M. L. Nieto and V. F. Puntes, *Angew Chem Int Edit*, 2004, **43**, 2538-2540.
18. J. Guzman, S. Carrettin and A. Corma, *J Am Chem Soc*, 2005, **127**, 3286-3287.
19. B. Murugan and A. V. Ramaswamy, *J Am Chem Soc*, 2007, **129**, 3062-3063.
20. W. I. Hsiao, Y. S. Lin, Y. C. Chen and C. S. Lee, *Chem Phys Lett*, 2007, **441**, 294-299.
21. C. W. Sun, H. Li, H. R. Zhang, Z. X. Wang and L. Q. Chen, *Nanotechnology*, 2005, **16**, 1454-1463.
22. R. J. La, Z. A. Hu, H. L. Li, X. L. Shang and Y. Y. Yang, *Mat Sci Eng a-Struct*, 2004, **368**, 145-148.
23. Y. F. Huang, Y. B. Cai, D. K. Qiao and H. Liu, *Particuology*, 2011, **9**, 170-173.
24. P. X. Huang, F. Wu, B. L. Zhu, X. P. Gao, H. Y. Zhu, T. Y. Yan, W. P. Huang, S. H. Wu and D. Y. Song, *J Phys Chem B*, 2005, **109**, 19169-19174.
25. R. J. Qi, Y. J. Zhu, G. F. Cheng and Y. H. Huang, *Nanotechnology*, 2005, **16**, 2502-2506.
26. D. E. Zhang, X. M. Ni, H. G. Zheng, X. J. Zhang and J. M. Song, *Solid State Sci*, 2006, **8**, 1290-1293.
27. M. Ge, C. S. Guo, L. Li, B. Q. Zhang, Y. C. Feng and Y. Q. Wang, *Mater Lett*, 2009, **63**, 1269-1271.
28. A. Vantomme, Z. Y. Yuan, G. H. Du and B. L. Su, *Langmuir*, 2005, **21**, 1132-1135.
29. C. S. Pan, D. S. Zhang and L. Y. Shi, *J Solid State Chem*, 2008, **181**, 1298-1306.
30. C. S. Pan, D. S. Zhang, L. Y. Shi and J. H. Fang, *Eur J Inorg Chem*, 2008, 2429-2436.
31. W. Q. Han, L. J. Wu and Y. M. Zhu, *J Am Chem Soc*, 2005, **127**, 12814-12815.
32. C. C. Tang, Y. Bando, B. D. Liu and D. Golberg, *Adv Mater*, 2005, **17**, 3005-3009.
33. K. B. Zhou, Z. Q. Yang and S. Yang, *Chem Mater*, 2007, **19**, 1215-1217.
34. Y. F. Yu, Y. M. Zhu, M. Meng, *Dalton Transaction*, 2013, **42**, 12087-12092.
35. J. W. Ko, J. H. Kim, C. B. Park, *J. Mater. Chem. A,* 2013, **1**, 241-245.
36. Z. X. Zhang, L. N. Wang, M. Shao, Y. L., G. L. Chen, J. Z. Shao, *Micro Nano Lett.,* 2012, **7**, 770-772.
37. L. Penn and J. F. Banfield, *Science*, 1998, **281**, 969-971. 38. J.C. Conesa, *Surface Science*, 1995, **339**, 337-352.
38. J.C. Conesa, *Surface Science*, 1995, **339**, 337-352.
39. S. Tsunekawa, J.T. Wang, Y. Kawazoe, A. Kasuya, *J. Appl. Phys.* 2003, **94**, 3654-3656.
40. M. Tamura, S. M. A. H. Siddiki, K. Shimizu, *Green Chemistry* **2013**, *15*, 1641-1646.